3D TCAD modeling of NO2CNT FET sensors

# 3D TCAD modeling of $NO_2$ CNT FET sensors

Stefania Carapezzi[1], Sebastian Eberle[2], Susanna Reggiani[1], Elena Gnani[1], Cosmin Roman[2], Christofer Hierold[2], Antonio Gnudi[1]
[1]University of Bologna (ARCES - DEI), V.le Risorgimento 2, 40136 Bologna, Italy
[2]Micro- & Nanosystems, Department of Mechanical and Process Engineering, ETH Zürich, Zürich, 8092, Switzerland
Email: stefania.carapezzi2@unibo.it

***Abstract*—A new approach for TCAD modeling of CNT FET gas sensors is presented, whose key feature is the use of an effective Gaussian DOS to mimic the 1D CNT DOS. The TCAD procedure has been applied to the simulation of a suspended CNT FET for $NO_2$ sensing. Our results indicate that the model is able to provide I-V characteristics in excellent agreement with the experimental data, both before and after gas exposure.**

## I. Introduction

Being all-surface objects exhibiting at the same time chemical, thermal and mechanical stability, carbon nanotubes (CNTs) are ideally suited to build highly sensitive, low-power and low-cost miniaturized gas sensors [1]. In [2] a device architecture based on a suspended CNT FET has been presented that offers the advantage of reduced power consumption, hysteresis-free operation and improved signal-to-noise ratio.

Modeling in general is extremely useful to improve the understanding of device operation and to assist device optimization. For CNT gas sensors in particular, the use of industry-level technology CAD (TCAD) tools is particularly attractive for their robustness and flexibility in handling complex 3D geometries. Moreover, as opposed to CNT FETs for nanoelectronic applications, in gas sensors the typical CNT lengths are of the order of micrometers, making the use of the TCAD diffusive transport approximation in the channel well justified (ballisticity is below 50% for a 300-nm long CNT [3]), while the typical measured conductances are orders of magnitude smaller than the quantum conductance limit.

On the other hand, commercial TCAD tools at present do not offer the possibility of modeling structures where the density-of-states (DOS) of carriers is markedly 1D, as indeed is the case in CNTs. This could explain why almost no TCAD modeling activity of CNT FETs has been reported in the literature (in [4] TCAD is used only to extract parasitic capacitances in CNT FETs).

The aim of the present work is to present an approach to 3D TCAD simulation of CNT FET gas sensors. The method is benchmarked against the experimental results presented in [5]. We show that after calibration of the main model parameters, a good match is obtained between experiments and simulations with and without gas exposure.

## II. TCAD modeling approach and device geometry

The starting point is the observation that, for the purpose of TCAD simulations, a semiconducting CNT can be modelled as a cylinder with the same diameter than the actual CNT and filled with a properly defined semiconductor material, provided the correct CNT electron linear density $n$ vs. Fermi-energy $E_F$ relationship is preserved. A fundamental difficulty here is that TCAD packages (SDevice by Synopsys [6] is used in this work) do not offer the option for a 1D electron-gas (1DEG) DOS model. The point is illustrated in Fig. 1(a), where the

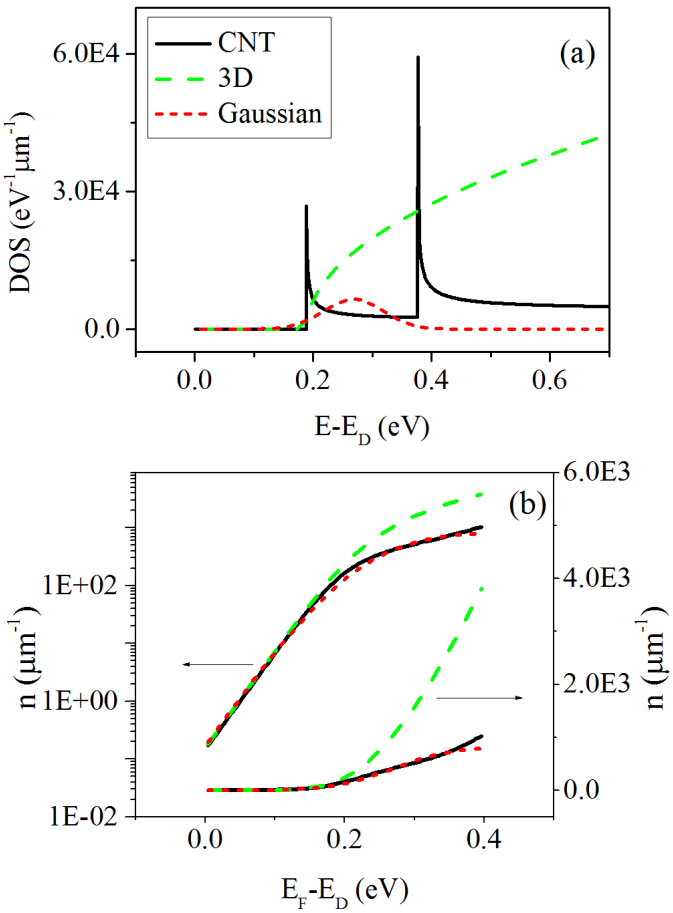


Fig. 1. (a) The first two subbands above the Dirac energy of the theoretical DOS of a zig-zag (26, 0) CNT (black solid line) are plotted together with the standard TCAD 3D DOS, integrated over the cylinder cross-section, of a semiconductor having the same energy gap and effective mass of the CNT first subband (green dashed line), and the calibrated Gaussian 3D DOS integrated over the cross-section (red short dashed line). (b) Electron densities $n$ vs. Fermi-energy $E_F$ corresponding to the above described DOS models.

theoretical DOS of a zig-zag (26, 0) CNT of 2-nm diameter [7] is compared with the TCAD 3D DOS integrated over the area of the cylindrical cross-section for a semiconductor having the same energy gap and first-subband effective mass as the CNT. This leads to a significantly inaccurate $n$-vs.-$E_F$ relationship, as shown in Fig. 1(b).

To circumvent the problem we decided to adopt the Gaussian 3D DOS model of SDevice, which exhibits a peaked-shape (see Fig. 1a). After calibration, such Gaussian DOS model provides an $n$-vs.-$E_F$ curve very similar to the target CNT one, as shown in Fig. 1(b), with an absolute relative error of less than 20% for $0 \leq E_F - E_D \leq 0.4$ eV. It should be noticed that only one Gaussian DOS is used in this work, mimicking only the first subband. This explains why the approximated $n$-vs.-$E_F$ curve tends to saturate at high $E_F$, while the CNT $n$ increases when $E_F$ enters the second subband. A second Gaussian DOS bump could be used to improve this aspect, but this is not necessary for the concentration levels relevant in experimental devices, as discussed below.

The residual $n$-vs.-$E_F$ error has very little impact on the overall simulation results, due to the suspended CNT topology with a thick air layer between the CNT and the gate (see Fig. 3). With reference to the vertical transverse cross-section shown in the inset of Fig. 2, the air-layer capacitance typically turns out to be much smaller than the CNT quantum capacitance, as calculated from the derivative of the $n$-vs.-$E_F$ curve of Fig. 1(b). For example, with $d_G = 200\,\text{nm}$ it follows $C_{\text{AIR}} = 0.0093\,\text{fF}/\mu\text{m}$ vs. $C_{\text{CNT}} \simeq 1\,\text{fF}/\mu\text{m}$. Since $C_{\text{AIR}}$ and $C_{\text{CNT}}$ are in series, the $n$-vs.-$V_{\text{GS}}$ relationship depends very little on the CNT capacitance, making the picture quite tolerant against small errors in the CNT DOS model, as shown in Fig. 2. From the figure it is also seen that the neglect of the second subband is responsible for the saturation of the Gaussian-DOS $n$ at high gate voltages, which however exceed the typical range utilized in experiments (see Fig. 4 and Fig. 5).

It should be noted that in Fig. 1(a) only the electron subbands and DOS are shown for simplicity, but actually in the TCAD simulations the CNT conduction and valence bands are modelled symetrically, so the above considerations apply to holes equally well.

The full device is modelled in TCAD with the 3D geometry shown in Fig. 3, which resembles the one in [5]. A CNT of 2-nm diameter and 2-$\mu$m length is anchored at both ends at the center of two supporting pillars. Each pillar consists of a layer of silicon dioxide (thickness 240 nm), capped with a 40-nm layer of palladium. At the bottom, another 40-nm layer of Pd lies between these pillars, making $d_G = 240\,\text{nm}$. The space between the supporting pillars below the CNT and up to 240 nm above the CNT is filled with an insulating material, whose relative permittivity is equal to 1 (air).

While in the real structure the pillars and the gate are several micrometers wide, in the simulated device the width $w_G$ has been set to four times $d_G$. It has been verified that this is enough to accurately model lateral electrostatic effects.

The standard SDevice Schottky contact model is used at the

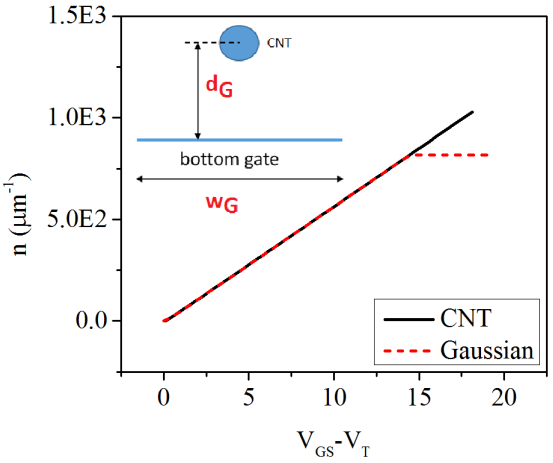


Fig. 2. Linear electron density $n$-vs.-$V_{\text{GS}}$ curves for the theoretical 1D DOS and the Gaussian 3D models plotted in Fig. 1(a). Inset: schematic of the vertical transverse cross-section of a suspended CNT FET; the full 3D geometry is illustrated in Fig. 3.

source/drain contacts. The contacted areas coincide with the two circular cross-sections at the two CNT ends. It is useful for the discussion in the next section to remind here the form of the Schottky contact boundary condition for the current continuity equation, which for holes (and similar for electrons) is

$$\mathbf{J}_p \cdot \hat{\mathbf{n}} = q\, v_{\text{p,rec}}(p - p_0), \tag{1}$$

where $\mathbf{J}_p$ is the hole current density vector, $\hat{\mathbf{n}}$ the unit vector normal to the contact surface pointing outward, $p$ the hole concentration at the contact, $v_{\text{p,rec}}$ the generation/recombination velocity for holes and $p_0$ the equilibrium hole concentration at the contact, which is fixed by the barrier height. At the source

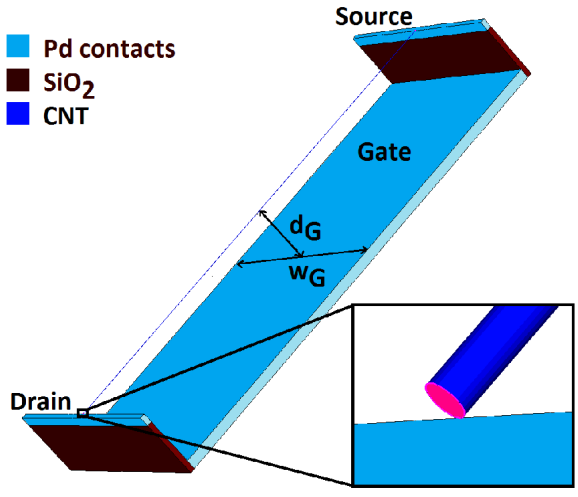


Fig. 3. The 3D geometry of the simulated suspended CNT FET. In the inset, the source region has been magnified. The contact region is highlighted in magenta.

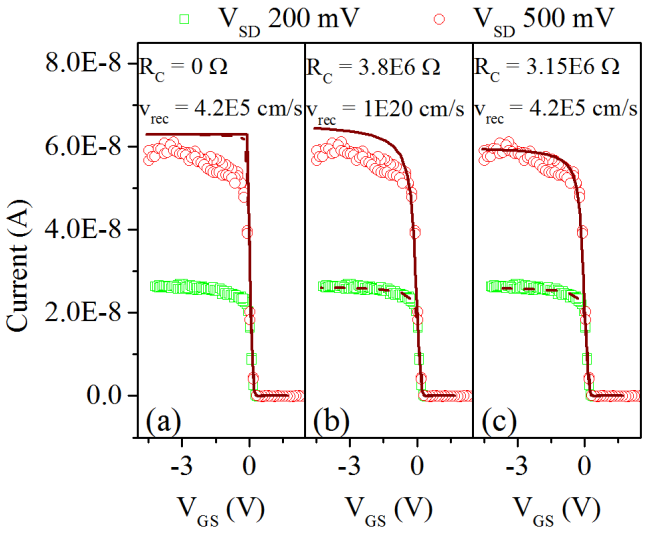


Fig. 4. (a)-(c) Experimental (empty symbols) and simulated transfer characteristics for $V_{\rm SD} = 0.2$ V and 0.5 V. In the simulated curves of (a), the contact resistance is set to zero and the recombination velocity is responsible for the saturation at high $V_{\rm GS}$. In (b), the recombination velocity is fixed to a very high value, and the current saturation is due only to the contact resistance. In (c) both the contact resistance and the recombination velocity are used to best match the experimental results.

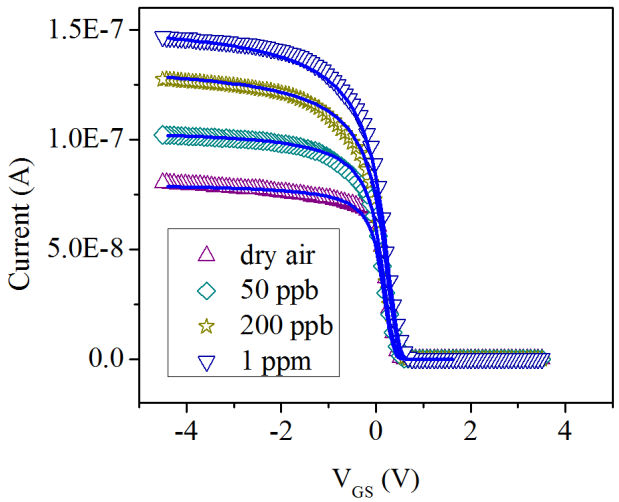


Fig. 5. Experimental (empty symbols) and simulated (solid lines) transfer characteristics of the CNT FET in dry air and in case of exposure to 50 ppb, 200 ppb and 1 ppm concentrations of $NO_2$. $V_{\rm SD} = 0.5$V.

contact holes are injected into the CNT and $p < p_0$, while at the drain contact holes are removed from the CNT and $p > p_0$.

It has been shown that the workfunction of single-walled zig-zag CNTs of diameter larger than 1 nm is very close to the one of graphene (4.55 eV) [8]. Therefore, such value has been adopted here. The workfunction of Pd has been set to 4.9 eV, which gives a slightly negative Schottky barrier height for holes equal to -0.16 eV. Actually, experimental results show that Pd creates near-Ohmic contacts to single-walled CNTs with diameter greater of 1.6 nm, while non-negligible positive Schottky barriers are found only for CNTs of diameter smaller than 1.6 nm [9].

The other model parameters are treated as adjustable parameters, following the procedure outlined in the next section.

## III. Results and Discussion

The first step is the consideration of the experimental $I_{\rm SD}$-$V_{\rm GS}$ characteristics in dry air, which are shown in Fig. 4 for two values of $V_{\rm SD}$, namely 0.2 V and 0.5 V. The measurements have been performed with one $V_{\rm GS}$ sweep in a fresh device, just after fabrication, and show almost no hysteresis. The current saturation at high negative $V_{\rm GS}$ is a strong indication of some injection limiting mechanism occurring at the contacts. Moreover, the fact that the saturation level significantly depends on the drain voltage suggests the presence of a sizable contact resistance. Indeed, a constant contact recombination velocity, which is part of the Schottky contact model as described above, can not explain, if considered alone, the $V_{\rm SD}$ dependence of the saturation current. This is illustrated in Fig. 4(a), which shows that the different simulated current curves saturate to the same value when there is no contact resistance. This can be understood from (1), which leads to a current saturation value independent of $V_{\rm SD}$ when $p << p_0$ at the source contact.

On the other hand, a constant contact resistance $R_C$ alone is not sufficient to model the experimental behavior. The simulated currents of Fig. 4(b), which have been obtained with a very high value of $v_{\rm p,rec}$ practically forcing $p = p_0$ in (1) and by adjusting the contact resistance so as to fit the $V_{\rm SD} = 0.2$ V saturation current, indicate that some additional current limiting mechanism must be invoked at $V_{\rm SD} = 0.5$ V. This mechanism can be found in the contact recombination velocity itself. The pair of values $R_C = 3.15 \times 10^6$ Ω and $v_{\rm p,rec} = v_{\rm n,rec} = 4.2 \times 10^5$ cm/s fits well the measured saturation currents for both $V_{\rm SD}$, as shown in Fig. 4(c). It should be noticed that in the simulation results of Fig. 4 the gate workfunction has been adjusted (using the same value for both $V_{\rm SD}$) in order to match the experimental threshold.

The CNT mobility value is mainly responsible for determining the slope of the linear part of the characteristics just above threshold and around the knee at the onset of current saturation. A spatially constant mobility model is used for simplicity. A good fitting with experiments (see Fig. 4(c)) is obtained with $\mu = 8 \times 10^3$ cm$^2$/Vs at $V_{\rm SD} = 0.2$ V and $\mu = 4 \times 10^3$ cm$^2$/Vs at $V_{\rm SD} = 0.5$ V. The smaller value at larger drain voltage can be due to a number of reasons, including the onset of velocity saturation in the CNT region close to the drain caused by the longitudinal electric field, or weak self-heating effects.

The second step is the consideration of the $I_{\rm SD}$-$V_{\rm GS}$ characteristics in the presence of $NO_2$. The experimental data shown in Fig. 5 correspond to averages taken at $V_{\rm SD} = 0.5$ V in the last ten minutes of an overall 1-hour exposure to different gas concentrations or in dry air. The $NO_2$ concentration impacts

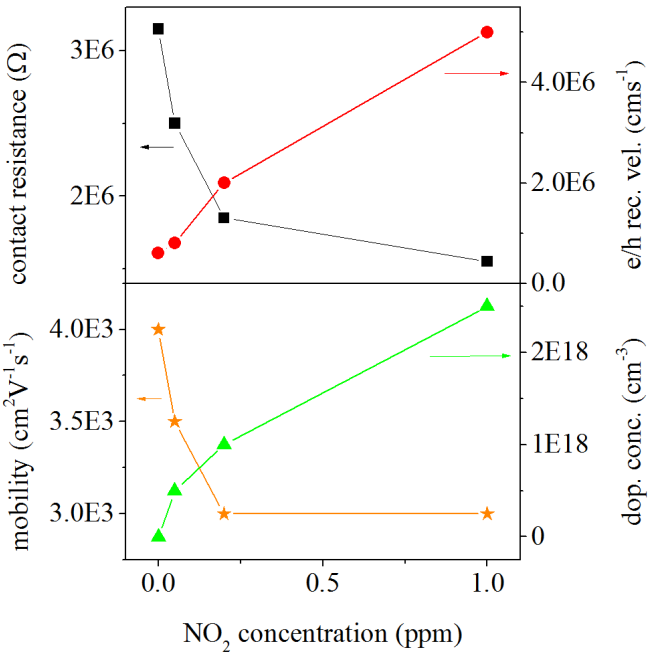


Fig. 6. Values of recombination velocity, contact resistance, *p*-doping concentration and mobility vs. $NO_2$ concentration resulting from best match between simulations and experimental data.

several aspects of the characteristics, primarily the saturation current, and to a lesser extent also the linear slope and the threshold voltage. Therefore, from the above discussion it appears that in the model the resistance and recombination velocity of the contacts, as well as the CNT mobility, have all to be made $NO_2$-concentration dependent. In addition, in order to mimic the $NO_2$ electron acceptor behavior, which effectively *p*-dopes the CNT channel, a spatially uniform *p*-doping concentration is introduced in the CNT, function of the gas concentration. In Fig. 5 the simulated currents are compared with the measured ones, while the extracted parameters vs. $NO_2$ concentration are collected in Fig. 6. Increasing the $NO_2$ concentration essentially causes a drop of the contact resistance and a nearly linear increase of the recombination velocity, both responsible for the variation of the saturation current. We believe that the increase of recombination velocity is related to the formation of recombination centers at the metal-CNT interfaces. An increasing trend not too far from linear is also exhibited by the effective doping level, corresponding to a rightward shift of the threshold voltage. Finally, the mobility tends to decrease with $NO_2$. We attribute this reduction to an increase with $NO_2$ of the hole scattering centers in the CNT. Our findings show that transfer characteristics are mostly controlled by contact properties, in partial agreement with [10].

## IV. Conclusion

In this abstract we have shown that a 3D TCAD modeling approach is able to explain with sufficient accuracy the current-voltage characteristics of suspended $NO_2$ CNT FET sensors. The main ingredients of the adopted approach are a non-standard semiconductor Gaussian DOS model to mimic the 1D CNT DOS and a resistive Schottky model for the source/drain contacts. Experimental transfer characteristics at different $V_{SD}$ in dry air and after exposure to different gas concentrations have been successfully reproduced, using the Schottky contact recombination velocity and resistance, as well as the channel mobility and effective doping concentration as adjustable parameters. We believe the proposed methodology will be helpful for future interpretation and optimization of this very promising type of gas sensor.

## Acknowledgment

The research leading to these results has been supported by 1) the Italian MIUR through EU H2020 FLAGERA JTC 2016 project CONVERGENCE "Frictionless Energy Efficient Convergent Wearables For Healthcare And Lifestyle Applications", via the IUNET Consortium, and 2) SNF-FLAG ERA CONVERGENCE (20FE-1_170224).

## References

[1] M. Mittal and A. Kumar, "Carbon nanotube (CNT) gas sensors for emissions from fossil fuel burning," *Sensors and Actuators B: Chemical*, vol. 203, pp. 349 – 362, 2014. [Online]. Available: http://www.sciencedirect.com/science/article/pii/S0925400514006091

[2] K. Chikkadi, M. Muoth, V. Maiwald, C. Roman, and C. Hierold, "Ultra-low power operation of self-heated, suspended carbon nanotube gas sensors," *Applied Physics Letters*, vol. 103, no. 22, p. 223109, 2013. [Online]. Available: https://doi.org/10.1063/1.4836415

[3] M. Pourfath, H. Kosina, and S. Selberherr, "Numerical study of quantum transport in carbon nanotube transistors," *Mathematics and Computers in Simulation*, vol. 79, no. 4, pp. 1051 – 1059, 2008, 5th Vienna International Conference on Mathematical Modelling/Workshop on Scientific Computing in Electronic Engineering of the 2006 International Conference on Computational Science/Structural Dynamical Systems: Computational Aspects. [Online]. Available: http://www.sciencedirect.com/science/article/pii/S0378475407002583

[4] C. Maneux, S. Fregonese, T. Zimmer, S. Retailleau, H. N. Nguyen, D. Querlioz, A. Bournel, P. Dollfus, F. Triozon, Y. M. Niquet, and S. Roche, "Multiscale simulation of carbon nanotube transistors," *Solid-State Electronics*, vol. 89, pp. 26 – 67, 2013. [Online]. Available: http://www.sciencedirect.com/science/article/pii/S0038110113002384

[5] S. Eberle, C. Roman, and C. Hierold, "Effect of varying gate distance on the threshold voltage shift in carbon nanotube field effect transistor gas sensors," *Microelectronic Engineering*, vol. 193, pp. 86 – 90, 2018. [Online]. Available: http://www.sciencedirect.com/science/article/pii/S0167931718300959

[6] *Sentaurus Device User Guide*, Synopsys Inc., Mountain View, CA, USA, 2014.

[7] T. Ando, "Theory of electronic states and transport in carbon nanotubes," *Journal of the Physical Society of Japan*, vol. 74, no. 3, pp. 777–817, 2005. [Online]. Available: https://doi.org/10.1143/JPSJ.74.777

[8] W. S. Su, T. C. Leung, and C. T. Chan, "Work function of single-walled and multiwalled carbon nanotubes: First-principles study," *Phys. Rev. B*, vol. 76, p. 235413, Dec 2007. [Online]. Available: https://link.aps.org/doi/10.1103/PhysRevB.76.235413

[9] W. Kim, A. Javey, R. Tu, J. Cao, Q. Wang, and H. Dai, "Electrical contacts to carbon nanotubes down to 1nm in diameter," *Applied Physics Letters*, vol. 87, no. 17, p. 173101, 2005. [Online]. Available: https://doi.org/10.1063/1.2108127

[10] J. Zhang, A. Boyd, A. Tselev, M. Paranjape, and P. Barbara, "Mechanism of NO2 detection in carbon nanotube field effect transistor chemical sensors," *Applied Physics Letters*, vol. 88, no. 12, p. 123112, 2006. [Online]. Available: https://doi.org/10.1063/1.2187510